ACS APPLIED ENERGY MATERIALS

www.acsaem.org Article

Carbon Nanotube/Reduced Graphene Oxide/Aramid Nanofiber Structural Supercapacitors

Anish Patel, Dimitrios Loufakis, Paraskevi Flouda, Ian George, Charles Shelton, John Harris, Suyash Oka, and Jodie L. Lutkenhaus*

Cite This: *ACS Appl. Energy Mater.* 2020, 3, 11763−11771 Read Online

ACCESS | Metrics & More | Article Recommendations | Supporting Information

ABSTRACT: Reduced graphene oxide/aramid nanofiber (rGO/ANF) supercapacitor electrodes have a good combination of energy storage and mechanical properties, but ion transport remains an issue toward achieving higher energy densities at high current because of the tightly packed electrode structure. Herein, carbon nanotubes (CNTs) are introduced to prevent rGO flake stacking to improve the rate capability of the rGO/ANF structural supercapacitor. The effect of CNTs on the rGO/ANF composite electrode's mechanical and electrochemical properties is investigated by varying the composition. The addition of 20 wt % CNTs led to an increase in Young's modulus up to 10.3 ± 1.8 GPa, while a maximum in ultimate strain and strength of 1.3 ± 0.14% and 55 ± 6.8 MPa, respectively, was found at a loading of 2.5 wt % CNTs. At low specific currents, the electrodes performed similarly (160−170 F g^{-1}), but at high specific currents (5 A g^{-1}), the addition of 20 wt % CNTs led to a significantly higher capacitance (76 F g^{-1}) as compared to that of rGO/ANF electrodes without CNTs (26 F g^{-1}). In addition, the energy density also improved significantly at high power from 1.4 to 5.1 W h L^{-1} with the addition of CNTs. The improvement in mechanical properties is attributed to the introduction of additional hydrogen-bonding and $\pi-\pi$ interactions from the carboxylic acid-functionalized CNTs. The increase in capacitance at higher discharge rates is due to improved ion transport from the CNTs. Finally, *in situ* electrochemomechanical testing examines how capacitance varies with strain in these structural electrodes for the first time.

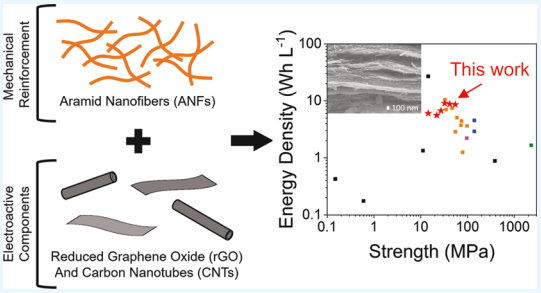

KEYWORDS: *aramid nanofibers, structural supercapacitor, electrochemomechanical, carbon nanotubes, multifunctional*

INTRODUCTION

Structural energy and power devices simultaneously store energy and bear mechanical loads. These multifunctional devices can allow for mass savings by replacing traditional structural components in applications such as electric vehicles, mobile electronics, and wearable electronics.[1−4] For example, a structural energy and power device may act as paneling for the wing of an unmanned aerial vehicle. However, the inherent trade-off between mechanical and electrochemical performances creates a significant challenge in fabricating multifunctional materials.[3−9] One common approach in structural energy and power material selection is to use either a composite material that consists of both structural and energy storage components or an inherently multifunctional material such as carbon fibers.[10−18]

Greenhalgh et al. fabricated carbon fiber-based structural supercapacitors that possessed a good compression strength (294.9 MPa) and modulus (52.0 GPa) but a poor specific capacitance (5 mF g^{-1}).[7] Elsewhere, structural batteries have been examined. Johannisson et al. developed a structural battery using carbon fibers and structural electrolyte with a longitudinal modulus of 52 GPa) and a good capacity (up to 232 mAh g^{-1}).[8] Meng et al. fabricated a structural nickel−iron battery that possessed a high Young's modulus (7.3 GPa) but a low specific energy (1.4 W h kg^{-1}).[19] Finally, Shi et al. designed an accordion-like lithium-ion battery that exhibited enhanced stretchability (up to 29%) while maintaining high energy density (233 W h L^{-1}).[20] While these results are promising, they often present a significant trade-off between mechanical and electrochemical performances or focus on flexibility instead of structural support.

Previous work from our group demonstrated the multifunctionality of a reduced graphene oxide (rGO) and aramid nanofiber (ANF) composite electrode for structural supercapacitors.[21] rGO is a two-dimensional nanosheet or flake that is commonly examined in supercapacitor electrodes for its excellent electrical conductivity and surface area, which results in a high reversible capacitance.[22−25] ANFs are high-aspect-ratio fibers derived from Kevlar thread that have demonstrated

Received: August 10, 2020
Accepted: October 30, 2020
Published: November 17, 2020

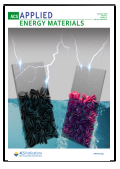

https://dx.doi.org/10.1021/acsaem.0c01926
ACS Appl. Energy Mater. 2020, 3, 11763−11771

exceptional mechanical enhancements when used as a filler for nanocomposites.[26−30] These structural electrodes performed well with an ultimate strength of 100 MPa and a specific capacitance of 120 F g^{-1} for an rGO/ANF electrode containing 25 wt % ANFs. With the goal of improving multifunctionality, or both mechanical and electrochemical performances, we further enhanced Young's modulus and strength of the rGO/ANF electrodes by installing hydrogen-bonding or coordination bonding functional groups on the rGO nanosheet's surface.[31−33]

While these results are promising in demonstrating an improved multifunctionality, this body of prior work highlights several challenges. First, the porosity of the electrode should be improved so as to facilitate energy storage at higher discharge rates and to improve accessibility of the electrolyte to the rGO nanosheet's surface. For example, interfacial interactions proved beneficial for the mechanical properties but resulted in a dense electrode that prevented electrolyte accessibility.[31−33] Second, the mechanical properties of the electrodes might be improved further by either increasing the ANF content or by selecting a third material bearing the desired mechanical properties. However, ANFs are electrochemically inactive and insulating, so increasing their presence (>20 wt %) causes severe reductions in capacitance.[21] Finally, the capacitance of rGO is limited due to rGO sheet agglomeration and consequent ion transport issues, which might be addressed by, again, adding a third active component.[34,35] Carbon nanotubes (CNTs) have been shown to improve the electrochemical performance of composite electrodes by facilitating electron transfer and by preventing agglomeration between rGO sheets.[36−39] Thus, we hypothesize that many of these advancements might be addressed by adding CNTs to the rGO/ANF electrode structure.

We are motivated by a cursory material informatics investigation, in which a ternary composite consisting of rGO, ANF, and CNTs exhibited improvements in both Young's modulus (increased by 78.8% to 18.9 GPa) and ultimate strength (increased by 34.4% to 66.3 MPa).[40] CNTs, a commonly used conductive component in supercapacitor electrodes, were chosen to prevent rGO sheet agglomeration and to allow for electrical connectivity between layers of rGO.[41−47] It was hypothesized that improving the through-plane electrical conductivity of the electrode and breaking up agglomeration of the rGO sheets would result in improved energy storage by promoting both ion diffusion and electron conduction. However, this approach was limited in that it did not examine the fundamental physical reasoning behind the suggested improvements due to CNTs in the composite. Further, this study, and many others in the area of structural energy power, did not examine the *in situ* response of the electrochemomechanical properties.

Herein, we study the effect of incorporating CNTs in rGO/ANF composite electrodes with the goal of improving electrochemical performance through the prevention of rGO sheet agglomeration. We systematically vary the CNT loading in graphene oxide (GO)/ANF/CNT dispersions and then fabricate supercapacitor electrodes using vacuum-assisted filtration and thermal reduction. These electrodes are then mechanically characterized using tensile testing and electrochemically characterized using cyclic voltammetry (CV), galvanostatic charge/discharge (GCD), and electrochemical impedance spectroscopy (EIS). This work is unique in that we also study the *in situ* mechanical and electrochemical properties.

MATERIALS AND METHODS

Materials. Kevlar thread was purchased from Thread Exchange. Carboxylic acid-functionalized CNTs were purchased from Cheap-Tubes. Graphite was purchased from Bay Carbon. Potassium permanganate ($KMnO_4$), sodium nitrate ($NaNO_3$), sulfuric acid (H_2SO_4), hydrochloric acid (HCl), hydrogen peroxide (H_2O_2), and dimethyl sulfoxide (DMSO) were purchased from Sigma-Aldrich. Potassium hydroxide (KOH) was purchased from Amresco. Deionized (DI) water was obtained by filtration through a Milli-Q system. Nylon membranes (47 mm diameter, 0.2 μm pores) were purchased from VWR.

Preparation of ANF Dispersion. ANF dispersions were prepared through the dissolution of Kevlar thread. Briefly, a mixture of 1 g of Kevlar thread, 1.5 g of KOH, and 500 mL of DMSO was stirred for 1 week. The resulting dark red dispersion was diluted to 0.2 mg mL^{-1} by adding DMSO.

Preparation of CNT Dispersion. The as-received CNTs were further functionalized with carboxylic acid groups and then dispersed in DMSO. Two hundred milligrams of CNTs were added to a mixture of 30 mL of HNO_3 (70%) and 90 mL of concentrated H_2SO_4. The mixture was stirred for 4 h at 60 °C and was then added to 800 mL of DI water. The mixture was stirred for 1 h and then vacuum-filtered through a nylon membrane. The CNTs were collected and redispersed in 300 mL of DI water. The mixture was then dialyzed to remove residual acid. Next, the mixture was dried in a conventional oven at 70 °C and then a vacuum oven at 80 °C to remove any residual water. Finally, the CNTs were collected and dispersed in DMSO at 0.2 mg mL^{-1}.

Preparation of GO Dispersion. The GO dispersion was prepared using a modified Hummers method. First, 3 g of graphite powder was added to 120 mL of cold, concentrated H_2SO_4 and 2.5 g of $NaNO_3$ while stirring for 5 h in an ice bath. Next, 15 g of $KMnO_4$ was slowly added over the course of 30 min while the temperature was kept below 20 °C using an ice bath. The mixture was stirred at 35 °C for 2 h and then added to 250 mL of DI water in an ice bath. After stirring for 20 min, the mixture was added to 700 mL of DI water and stirred for 20 min. Next, 20 mL of 30 wt % H_2O_2 was added to the mixture and was then stirred for another 20 min. The mixture turned brown upon the addition of H_2O_2. One liter of 5 wt % HCl was added to the mixture, which was then stirred overnight. The oxidized graphite was collected using vacuum filtration and dispersed in 250 mL of DI water. The dispersion was dialyzed to remove impurities and residual acid. The dispersion was filtered, and the collected graphite oxide was dried under vacuum at 60 °C for 6 h. 200 mg of graphite oxide powder was then dispersed in 100 mL of DI water and ultrasonicated for 1 h to yield GO. Finally, 200 mL of DMSO was added to the mixture and the water was removed using rotary evaporation yielding a 1.0 mg mL^{-1} dispersion of GO in DMSO.

Fabrication of rGO/ANF/CNT Electrodes. rGO/ANF/CNT electrodes were fabricated using vacuum-assisted filtration and thermal reduction. First, the GO and CNT dispersions were bath-sonicated for 1 h. Next, the ANF, CNT, and GO dispersions were mixed in the desired ratios (Table 1) and stirred for 1 h. The total solid mass in the mixture was kept at 40 mg, and the mass ratio of ANF to GO was held to 1:19 for all vacuum-filtered electrodes. Previous work in our lab indicated that this ratio was ideal for high multifunctionality.[21] The amount of CNT dispersion added was varied to obtain electrodes with 0−20 wt % CNTs. Higher CNT content was not explored to avoid having too little mechanical nanofiller or too little rGO, which provides more energy storage. After stirring, DI water was added to the mixture (1 mL of DI water for every 1 mg of ANF) and the mixture was heated to 80 °C and stirred for 2 h. The mixture was then cooled to 40−50 °C and vacuum-filtered through a nylon membrane. The electrode was then washed in DI water twice and air-dried for 30 min. The electrode was peeled from the nylon membrane, placed in between two glass slides to

https://dx.doi.org/10.1021/acsaem.0c01926
ACS Appl. Energy Mater. 2020, 3, 11763−11771

Table 1. Composition of Electrodes (in wt %) Used in This Study with the Amount of Material (in mg) Used during the Dispersion Step in Parentheses

rGO content wt % (mg)	ANF content wt % (mg)	CNT content wt % (mg)	Referred to as
95 (38)	5 (2)	0 (0)	95/5/0 rGO/ANF/CNT
92.6 (37.05)	4.9 (1.95)	2.5 (1)	92.6/4.9/2.5 rGO/ANF/CNT
90.3 (36.1)	4.7 (1.9)	5 (2)	90.3/4.7/5 rGO/ANF/CNT
85.5 (34.2)	4.5 (1.8)	10 (4)	85.5/4.5/10 rGO/ANF/CNT
80.8 (32.3)	4.2 (1.7)	15 (6)	80.8/4.2/15 rGO/ANF/CNT
76 (30.4)	4 (1.6)	20 (8)	76/4/20 rGO/ANF/CNT

prevent wrinkling, and dried under vacuum at 80 °C for 3 days. The electrodes were cut into the desired shapes for characterization. Finally, thermal reduction was used to reduce GO to rGO. The GO/ANF/CNT electrodes were thermally reduced under vacuum at 200 °C for 2 h to yield rGO/ANF/CNT electrodes. During reduction, the electrodes were placed between heavy tiles to prevent bubble formation. The final compositions for the electrodes are listed in Table 1, and the electrode density is listed in Table S1. The nomenclature "rGO/ANF/CNT" represents the relative mass fractions of the respective components.

Electrode Characterization. The morphology of the electrodes was characterized using scanning electron microscopy (SEM, JEOL JSM-7500F) and transmission electron microscopy (TEM, JEOL JEN-2010). Atomic force microscopy (AFM) images of rGO flakes were obtained on a Bruker Dimension Icon AFM in tapping mode. X-ray photoelectron spectroscopy (XPS) was used to confirm the reduction process. XPS spectra were obtained on an Omicron ESCA Probe (Omicron Nanotechnology) with a monochromated Mg Kα radiation (1253.6 eV). XPS survey scans were performed with an analyzer pass energy of 100−1100 eV (1.0 eV steps, 50 ms dwell time), while high-resolution scans of carbon (C 1s) and nitrogen (N 1s) were performed with a pass energy of 150 eV (0.05 eV steps, 200 ms dwell time). All spectra were calibrated with the C 1s photoemission peak for sp^2-hybridized carbons at 284.5 eV and the FWHM was constrained. Curve fitting of C 1s and N 1s spectra was conducted using a Gaussian−Lorentzian peak shape after Shirley-type background correction. X-ray diffraction (XRD) was used to confirm the reduction process and to examine layer spacing with increased CNT content. XRD spectra were obtained using an X-ray diffractometer (Bruker-AXS D8 Advance) with Cu Kα (λ = 1.541 Å) and 2θ range of 5−50°. Raman spectra were obtained on a Horiba Jobin-Yvon LabRam HR Raman Spectrometer.

Mechanical Characterization. Tensile testing was conducted using a dynamic mechanical analyzer (DMA, TA Instruments Q800) in thin film tensile mode. Electrodes were cut into rectangular shapes prior to reduction with a length of ~10 mm and a width of ~2.5 mm. Thickness was obtained using a height gauge (TESA μ-hite). Electrodes were clamped with a preload force of 0.02 N and then strained at a strain rate of 0.1% min^{-1} until failure. Three to five samples were tested per composition.

Electrochemical Characterization. Through-plane electronic conductivity was obtained using electrochemical impedance spectroscopy (EIS). The electrodes were placed between two stainless steel blocking electrodes in a Tom cell with no electrolyte. Conductivity when immersed in electrolyte was also obtained using EIS. A symmetric Tom cell was assembled using two electrodes, carbon paper as the current collector, and 400 μL of 6 M KOH as the electrolyte. A perturbation voltage of 10 mV was used at the open-circuit potential with a frequency range of 5 mHz to 1 MHz. A control coin cell consisting of only stainless steel electrodes was used to obtain the resistance of the cell and connectors.

Electrochemical performance was evaluated using a symmetric coin cell with 6 M KOH and Celgard 3501 as the separator. Cyclic voltammetry was performed with a voltage range of 0−1 V at 1, 5, 10, 20, 50, 100, and 200 mV s^{-1}. Galvanostatic charge/discharge measurements were conducted at a voltage window of 0 to 1 V. Rate capability studies used specific currents of 0.1, 0.5, 1, and 5 A g^{-1}. eq 1 was used to calculate capacitance from cyclic voltammetry, and eq 2 was used to calculate capacitance from galvanostatic charge/discharge. C is the capacitance, I is the specific current, ΔV is the voltage window, v is the scan rate, m is the total electrode mass, and Δt is the discharge time. Finally, the electrodes' cycling stabilities were characterized by cycling the symmetric coin cell for 5000 cycles at 0.5 A g^{-1}.

$$C = \frac{2\int i\,dV}{v\Delta V m} \quad (1)$$

$$C = \frac{4I\Delta t}{\Delta V} \quad (2)$$

In situ testing was conducted using a three-dimensional (3D)-printed cell that allowed the electrode to be in contact with a 6 M KOH electrolyte while being clamped to a tensile stage. Silver wires were attached to the electrode and connected to a Gamry Interface 1000 for electrochemical testing. A symmetric rGO/ANF/CNT electrode was used as the counter/reference electrode.

RESULTS AND DISCUSSION

rGO/ANF/CNT electrodes were fabricated using vacuum-assisted filtration and thermal reduction for 2 h at 200 °C. The electrodes are designated by their composition (see Table 1), where the electrode name indicates the mass fraction of each component. SEM images (Figure 1a,b and Figures S1 and S2) show that the resulting electrodes possessed a well-layered structure, where rGO flakes lay parallel to the substrate, and ANFs and CNTs appear between the rGO flakes. High-resolution SEM images in Figure S1 confirm the presence of CNTs in the 76/4/20 rGO/ANF/CNT electrode. rGO flakes were 0.2−0.55 nm in thickness and 150−600 nm in lateral size (Figure S3). From prior work, ANFs are 30−40 nm in diameter and 5−10 μm in length.[48] CNTs are 13−18 nm in diameter and 3−30 μm in length,[49] confirmed by the TEM image shown in Figure 1c.

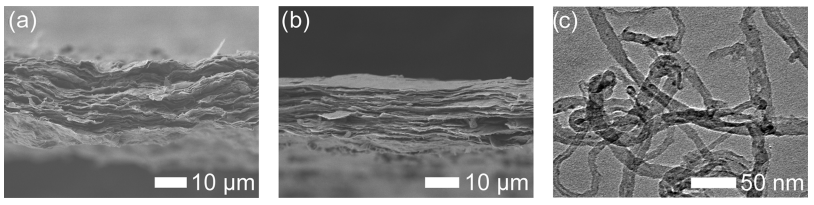

Figure 1. Cross-sectional SEM images of (a) 95/5/0 and (b) 76/4/20 rGO/ANF/CNT electrodes. (c) Transmission electron micrograph of drop-casted CNTs.

https://dx.doi.org/10.1021/acsaem.0c01926
ACS Appl. Energy Mater. 2020, 3, 11763−11771

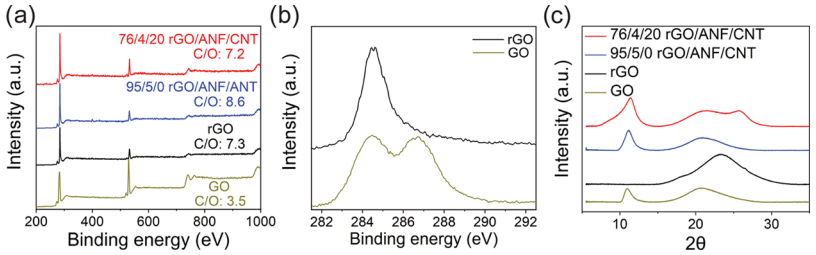

Figure 2. (a) XPS survey scans, (b) high-resolution C 1s spectra, and (c) XRD spectra for GO (gray), rGO (black), 95/5/0 (blue), and 76/4/20 (red) rGO/ANF/CNT electrodes.

XPS was used to verify the thermal reduction of GO to rGO. The carbon-to-oxygen ratio (C/O ratio) (Figure 2a) increased from 3.5 for GO to 7.3 for rGO, which confirms the loss of oxygen-containing groups on GO. In addition, high-resolution C 1s spectra (Figure 2b) show the disappearance of the peak attributed to oxygen groups at ∼286.1 eV. XPS also indicated the presence of ANFs and CNTs within the rGO/ANF/CNT electrodes. High-resolution N 1s spectra (Figure S5a−c) indicate a lack of nitrogen in a pure rGO electrode (without ANFs) and an appearance of nitrogen in both 95/5/0 and 76/4/20 rGO/ANF/CNT electrodes, confirming the presence of ANFs. High-resolution C 1s spectra (Figure S5d−g) show an increase in the peak area associated with carboxylic acid groups for the 76/4/20 rGO/ANF/CNT electrodes, arising from the CNT's -COOH functional groups. Finally, Raman spectroscopy also confirmed the reduction of GO to rGO with a decrease in ratio of the D-to-G band intensities from 1.12 to 0.97 (Figure S4).

XRD was used to examine the effect of CNTs on the interlayer spacing in the composite electrodes (Figure 2c). The unreduced electrodes were examined here because resolving the peaks affiliated with the interlayer spacing in reduced electrodes proved difficult. The d-spacing of the GO electrode was 8.0 Å, whereas the d-spacing of the composite electrodes ranged from 7.1 to 7.9 Å with no clear trend in composition. This is likely because rGO exists as flakes, rather than individual sheets, and the ANFs and CNTs reside between flakes (not sheets).

Stress−strain curves were obtained from tensile testing of the composite electrodes to estimate Young's modulus, ultimate strain, and ultimate strength (Figure 3 and Table S1). Overall, there was no clear trend with composition in the mechanical properties, but we observe a few interesting features. First, the highest Young's modulus (10.3 ± 1.8 GPa) occurred for the electrodes containing the largest amount of CNTs (76/4/20 rGO/ANF/CNT). Second, the highest ultimate strain (1.3 ± 0.14%) and ultimate strength (55 ± 6.8 MPa) were obtained for 92.6/4.9/2.5 rGO/ANF/CNT electrodes, which possessed an intermediate CNT composition. Finally, the poorest mechanical properties resulted from 90.3/4.7/5 rGO/ANF/CNT composite electrode, having Young's modulus, ultimate strain, and ultimate strength of 3.4 ± 0.6 GPa, 0.5 ± 0.10%, 14 ± 2.9 MPa, respectively. These results show that adding CNTs (up to 2.5 wt %) to the rGO/ANF electrode improves the mechanical properties.

We compare here these results with our past work on pure rGO electrodes that possessed Young's modulus, ultimate strain, and ultimate strength of 3.7 ± 0.4 GPa, 1.0 ± 0.1%, and 34.4 ± 0.1 MPa, respectively.[21] Here, the incorporation of both ANFs and CNTs resulted in a 200% increase in Young's

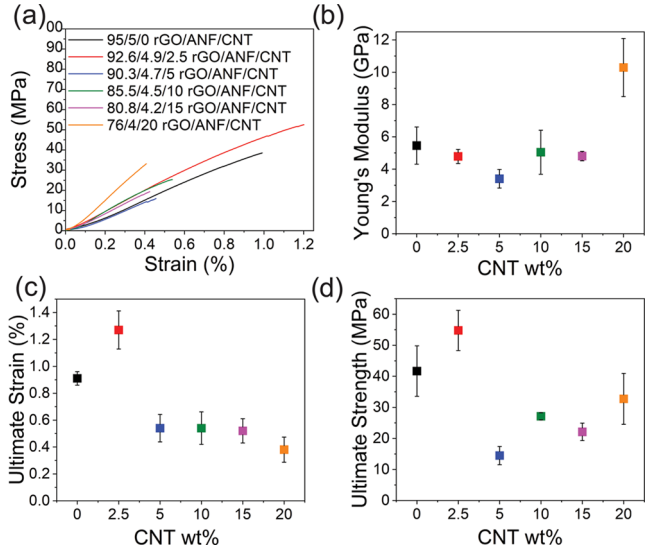

Figure 3. (a) Representative stress−strain curves, (b) Young's modulus, (c) ultimate strain, and (d) ultimate strength for 95/5/0 (black), 92.6/4.9/2.5 (red), 90.3/4.7/5 (blue), 85.5/4.510 (green), 80.8/4.2/15 (purple), and 76/4/20 (orange) rGO/ANF/CNT electrodes. The error bars represent the standard deviation of three to five experiments.

modulus, a 30% increase in ultimate strain, and a 62% increase in ultimate strength compared to 92.6/4.9/2.5 rGO/ANF/CNT. For further comparison, rGO/ANF electrodes showed mechanical performance intermediate to that of pure rGO vs rGO/ANF/CNT electrodes.

The reason for the rGO/ANF/CNT electrode's improved mechanical properties is attributed to enhanced interfacial interactions that accommodate load transfer. For example, there are hydrogen-bonding interactions among the COOH-functionalized CNTs, ANFs, and oxygen-containing functional groups on the rGO nanosheet surface. There also exists $\pi-\pi$ stacking among the three components, further enhancing the interfacial bonding.[21,48,50−52] The benefit of adding CNTs was observed up to 2.5 wt % for which the ultimate strain and strength were increased (but Young's modulus remained fairly constant). At higher CNT loadings, the electrode became more brittle as the modulus increased, but the strain and strength generally decreased. This may possibly indicate a shift from hydrogen-bonding (∼320 meV)[51] and $\pi-\pi$ interactions (∼50−90 meV)[50] among the three components to $\pi-\pi$ interactions dominating among the CNTs and rGO nanosheets.

We next considered the electronic properties of the composite electrodes because conductivity impacts electrochemical performance. Through-plane conductivity (Figure 4)

https://dx.doi.org/10.1021/acsaem.0c01926
ACS Appl. Energy Mater. 2020, 3, 11763−11771

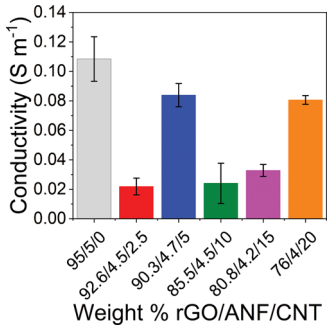

Figure 4. Through-plane electronic conductivity for 95/5/0, 92.6/4.9/2.5, 90.3/4.7/5, 85.5/4.510, 80.8/4.2/15, and 76/4/20 rGO/ANF/CNT electrodes.

was obtained using EIS in a coin cell configuration composed of two stainless steel blocking electrodes with no electrolyte. The electronic conductivity for the rGO/ANF/CNT electrodes ranged from 0.02 to 0.11 S m^{-1} with no clear trend with composition, where 95/5/0 rGO/ANF/CNT showed the highest conductivity. However, the addition of CNTs led to a decrease in electronic conductivity. This may be attributed to the highly functionalized CNTs, where carboxylation introduces defects in the sp^2-hybridized carbon lattice. This is supported by Raman spectroscopy (Figure S4), which revealed an increasing ratio of D-to-G band intensities as CNT content increased (from 0.95 for 95/5/0 rGO/ANF/CNT to 1.21 for 76/4/20 rGO/ANF/CNT). Also, the CNTs introduce contact resistance, which may decrease the overall electronic conductivity.

Electrochemical testing was carried out using a two-electrode symmetric coin cell with 6 M KOH as the electrolyte (Table S1). CV was performed between 0 and 1 V at varying scan rates (Figure 5a). At a scan rate of 0.001 V s^{-1}, the specific capacitance decreased with increasing CNT content, from 169 to 134 F g^{-1} for 95/5/0 to 76/4/20 rGO/CNT/ANF, respectively. However, at a scan rate of 0.2 V s^{-1}, the specific capacitance showed a maximum with a CNT content of 5 wt % (79 F g^{-1} for 90.3/4.7/5 rGO/ANF/CNT).

Galvanostatic cycling was used to examine rate capability and cycling stability (Figure 5c,d and Figure S9). For rate capability testing, all electrodes exhibited a decrease in capacitance retention as specific current increased, which was attributed to diffusion limitations. However, similar to CV results, the capacitance retention increased with the addition of CNTs, for which the electrode with the highest CNT loading (76/4/20 rGO/ANF/CNT) exhibited the highest capacitance retention. Specifically, for 95/5/0 rGO/ANF/CNT, the capacitance retention was only 19.4 ± 0.7% for increasing specific current from 0.1 to 5.0 A g^{-1}. For 76/4/20 rGO/ANF/CNT, the capacitance retention was 58.3 ± 0.1%. At the highest specific current evaluated (5 A g^{-1}), 76/4/20 rGO/ANF/CNT electrodes had a capacitance 190% higher than that for 95/5/0 rGO/ANF/CNT electrodes (75.8 ± 0.2 vs 26.2 ± 1.0 F g^{-1}, respectively), emphasizing the important role of CNTs in promoting charge storage. The inclusion of CNTs allows for greater capacitance at both higher scan rates and faster charge/discharge rates. For long-term cycling stability, the rGO/ANF/CNT electrodes possessed capacitance retentions ranging from 87.1 to 96.6% at 5000 cycles. The 95/5/0 rGO/ANF/CNT electrodes possessed the worst capacitance retention, whereas the addition of CNTs improved capacitance retention up to 96.6% for the 76/4/20 rGO/ANT/CNT electrode. The initial increase in capacitance retention can be attributed to insufficient preconditioning, and the decrease at later cycles is likely due to electrode degradation that might result from changes in the pore structure during cycling.

Together, these results highlight the beneficial role of CNTs in promoting charge storage in the rGO/ANF composite electrodes. The question is, then, what CNT loading is required to gain or retain these benefits. Without CNTs, the composite electrodes exhibited the lowest capacitance and capacitance retention. The addition of up to 2.5 wt % CNTs

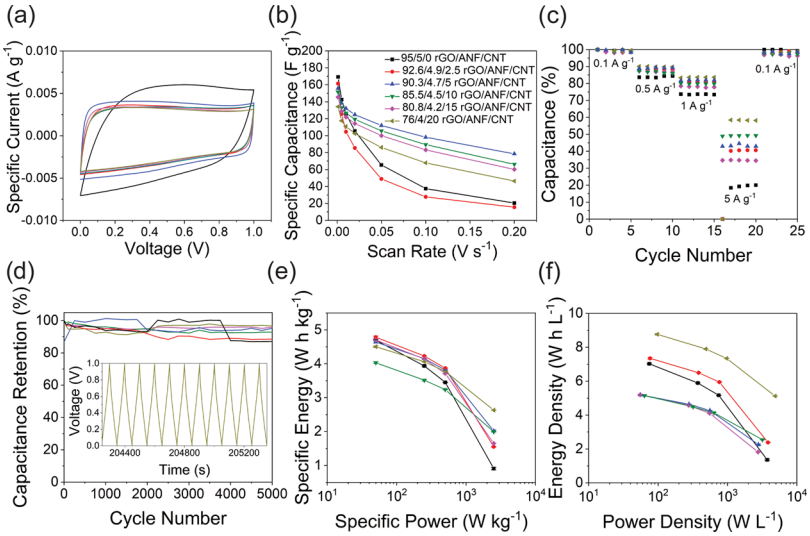

Figure 5. (a) Typical CV curves at 0.01 V s^{-1}, (b) specific capacitance vs scan rate, (c) rate capability during charge/discharge, (d) cycling stability up to 5000 cycles with an inset showing the charge/discharge curves for cycles 2000−2010 of 76/4/20 rGO/ANF/CNT, and Ragone plots of (e) specific energy vs specific power and (f) energy density vs power density for electrodes with varying CNT loading. The legend in (b) applies to all other figures: 95/5/0 rGO/ANF/CNT in black squares, 92.6/4.9/2.5 rGO/ANF/CNT in red circles, 90.3/4.7/5 rGO/ANF/CNT in blue triangles (pointing up), 85.5/4.5/10 rGO/ANF/CNT in green triangles (pointing down), 80.8/4.2/15 rGO/ANF/CNT in purple diamonds, and 76/4/20 rGO/ANF/CNT in yellow triangles (pointing left).

https://dx.doi.org/10.1021/acsaem.0c01926
ACS Appl. Energy Mater. 2020, 3, 11763−11771

did not significantly affect the capacitance of the electrode at varying scan rates. However, a higher CNT loading (> 5 wt %) drastically improved the rate capability of the electrodes (Figure 5b). As for discharge capacitance, electrodes containing 5 wt % CNTs exhibited the highest capacitance in CV measurements, but those containing 20 wt % CNTs performed best in galvanostatic charge/discharge measurements and cycle stability, especially with regard to energy and power density. Considering that capacitors are more practically operated under galvanostatic conditions, we place higher emphasis on results obtained under those conditions. All together, these results suggest that CNTs alleviate mass diffusion limitations that are more prevalent at higher scan rates or discharging rates. The CNTs might be lending more porosity to the overall electrode by separating rGO flakes from one another. This idea is supported by the lower electrical resistance of 76/4/20 rGO/ANF/CNT electrodes when immersed in electrolyte (6800 ± 160 Ω) as compared to that of 95/5/0 rGO/ANT/CNT electrode without CNTs (8100± 140 Ω); see the EIS of full cells in Figure S6. This result indicates that CNTs enhance either the number of pores or the pore size by preventing aggregation of rGO flakes.

In the preceding results, we observed that CNT additives yielded improved capacitance and capacitance retention for rGO/ANF-based electrodes due to a likely increase in porosity, but mechanical properties did not follow the same trend. For a multifunctional application, a trade-off in electrochemical and mechanical performances is expected; thus, it is important to identify some optimal combination of the two desired properties. Accordingly, the Ashby plot in Figure 6 compares

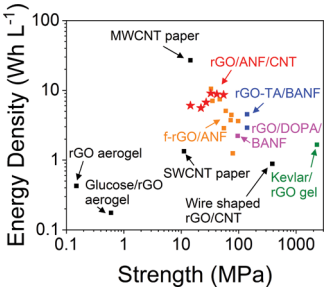

Figure 6. Ashby plot with energy density vs strength for this work and electrodes from the literature. Table S3 summarizes the values shown.

the energy density and ultimate strength of the electrodes in this work (red stars) with other structural electrodes in the literature.[31−33,53−69] When compared to other supercapacitors, the rGO/ANF/CNT electrodes performed well with both a good energy density and strength. When compared to similar materials from our group (purple, blue, and orange squares), this work showed a slight improvement in energy density at a small cost in strength. Figure S7 shows Ashby plots comparing specific energy, capacitance, and strength.

Finally, *in situ* testing of the electrodes (Figure 7) was conducted using a custom-built tensile stage in conjunction with a potentiostat. A schematic representation of the *in situ* setup is shown in Figure 7a. The working electrode is attached to tension clamps and the potentiostat while in contact with the electrolyte. The overall configuration was a two-electrode capacitor in which a second identical sample was used to complete the electrochemical circuit. The capacitance retention of the electrode was measured at different strains on the electrode to evaluate the electrode's ability to store energy under mechanical loads. In addition, a tensile test was performed while the electrode was charged and discharged to evaluate the electrode's mechanical performance while being cycled. Digital image correlation (DIC) was conducted to confirm the lack of grip slip (Figure S8). The 92.6/4.9/2.5 rGO/ANF/CNT electrode composition was chosen as it possessed the best mechanical performance.

The capacitance of the electrode was tested initially under no strain. Next, the electrode was stretched at 0.2% strain intervals until failure. At each interval and after failure, the capacitance was again measured and compared against the initial capacitance (Figure 7b). The capacitance retention for the 92.6/4.9/2.5 rGO/ANF/CNT electrode at failure was 60.8 ± 16.4%. Next, the electrode was strained at 0.2% strain intervals again with three charge/discharge cycles at 50 mV/s in between until failure (Figure 7c). The sharp drop in stress at each interval is due to electrolyte uptake and potential structural changes in the electrode during the charge and discharge cycles. These structural changes are not accounted for when calculating stress. The resulting Young's modulus, ultimate strength, and ultimate strain during cycling for the 92.6/4.9/2.5 rGO/ANF/CNT electrode were 740 ± 230 MPa, 7.6 ± 1.2 MPa, and 1.2 ± 0.62%, respectively. The rGO/ANF/CNT electrode retains ∼75% of its capacitance despite being stretched up to 0.8% strain (∼66% of the ultimate strain). This indicates that the electrode can store energy despite being under significant strain. However, Young's modulus and ultimate strength decreased drastically under *in situ* testing conditions as compared to those under dry conditions (Young's modulus = 4.8 ± 0.4 GPa and ultimate strength = 54.8 ± 6.5 MPa for the dry electrode; Figure 3). We speculate that this reduction is attributed to plasticization from the aqueous electrolyte. However, the ultimate strain was unchanged from the dry state despite immersion in electrolyte and charge/discharge cycling. From these results, it is clear that

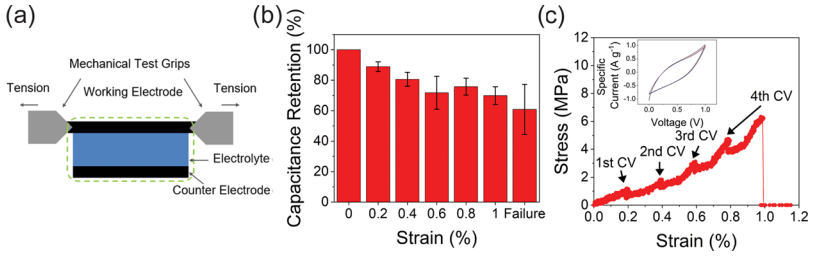

Figure 7. (a) Schematic representation of the *in situ* testing setup (side view). (b) Capacitance retention of the composite electrode at different strains and (c) the stress−strain curve during electrochemical cycling with three charge/discharge cyclic voltammetry (CV) cycles (fourth set of CV curves shown in the inset) at every 0.2% strain interval.

https://dx.doi.org/10.1021/acsaem.0c01926
ACS Appl. Energy Mater. 2020, 3, 11763−11771

the structural electrode can store energy and withstand high strains under mechanical deformation and charging/discharging, respectively.

CONCLUSIONS

Improved structural electrodes were successfully fabricated using a combination of rGO, ANFs, and CNTs. The addition of CNTs improved electrolyte accessibility by preventing rGO sheet agglomeration and by probably increasing the number of pores or size of pores, resulting in improved capacitance retention and energy density. With the incorporation of 2.5 wt % CNTs, improvements in ultimate strength and strain were realized relative to similar electrodes without CNTs. However, higher CNT loadings (20 wt %) resulted in increased brittleness with a higher Young's modulus. This may possibly be ascribed to a shift to weaker $\pi-\pi$ interactions (CNT−CNT and CNT−rGO contacts) from stronger hydrogen-bonding interactions (ANF−CNT, ANF−rGO) as the CNT content increased. Overall, the rGO/ANF/CNT electrodes possessed a good trade-off of electrochemical and mechanical properties with improved capacitance as compared to previous work on rGO/ANF electrodes (without CNTs). Finally, the rGO/ANF/CNT electrodes demonstrated improved capacitance retention and mechanical performance under *in situ* conditions.

Looking at the future, new approaches are needed to develop structural electrodes that significantly increase the specific energy and power further without sacrificing modulus or strength. As noted, rGO-based supercapacitors are limited in capacitance due to mass diffusion limitations that arise from rGO sheet stacking. One way to mitigate this is to engineer highly porous, 3D rGO networks with high surface area and sufficient porosity for improved energy storage, but mechanical properties often suffer.[70] Our future work may focus upon combining the mechanical robustness of carbon fiber supercapacitors[2,7] with the concepts learned herein to balance energy, power, and mechanical properties through design of the electrode's morphology, density, and porosity.

ASSOCIATED CONTENT

Supporting Information

The Supporting Information is available free of charge at https://pubs.acs.org/doi/10.1021/acsaem.0c01926.

Tabulated properties, SEM images, AFM images, high-resolution XPS, equivalent circuits for EIS, additional Ashby plots, and DIC (PDF)

AUTHOR INFORMATION

Corresponding Author

Jodie L. Lutkenhaus − *Artie McFerrin Department of Chemical Engineering and Department of Materials Science and Engineering, Texas A&M University, College Station, Texas, United States;* orcid.org/0000-0002-2613-6016; Email: jodie.lutkenhaus@tamu.edu

Authors

Anish Patel − *Artie McFerrin Department of Chemical Engineering, Texas A&M University, College Station, Texas, United States*

Dimitrios Loufakis − *Department of Materials Science and Engineering, Texas A&M University, College Station, Texas, United States*

Paraskevi Flouda − *Department of Materials Science and Engineering, Texas A&M University, College Station, Texas, United States*

Ian George − *Artie McFerrin Department of Chemical Engineering, Texas A&M University, College Station, Texas, United States*

Charles Shelton − *Department of Chemical and Materials Engineering, University of Alabama Huntsville, Huntsville, Alabama, United States*

John Harris − *Artie McFerrin Department of Chemical Engineering, Texas A&M University, College Station, Texas, United States*

Suyash Oka − *Artie McFerrin Department of Chemical Engineering, Texas A&M University, College Station, Texas, United States*

Complete contact information is available at: https://pubs.acs.org/10.1021/acsaem.0c01926

Author Contributions

The manuscript was written through contributions of all authors. All authors have given approval to the final version of the manuscript.

Funding

This work was supported in part by the Air Force Office of Scientific Research (grant number FA9550-19-1-0170).

Notes

The authors declare no competing financial interest.

ACKNOWLEDGMENTS

Use of the TAMU Materials Characterization Facility and the TAMU Microscopy & Imaging Center is acknowledged. J.L. acknowledges support as holder of the Axalta Chair.

REFERENCES

(1) O'Brien, D.; Baechle, D.; Wetzel, E. Design and performance of multifunctional structural composite capacitors. *J. Compos. Mater.* **2011**, *45*, 2797−2809.

(2) Asp, L. E.; Greenhalgh, E. S. Structural power composites. *Compos. Sci. Technol.* **2014**, *101*, 41−61.

(3) Asp, L. E.; Johansson, M.; Lindbergh, G.; Xu, J.; Zenkert, D. Structural battery composites: a review. *Funct. Compos. Struct.* **2019**, *1*, No. 042001.

(4) Qian, G.; Liao, X.; Zhu, Y.; Pan, F.; Chen, X.; Yang, Y. Designing Flexible Lithium-Ion Batteries by Structural Engineering. *ACS Energy Lett.* **2019**, *4*, 690−701.

(5) Snyder, J. F.; Wetzel, E. D.; Watson, C. M. Improving multifunctional behavior in structural electrolytes through copolymerization of structure-and conductivity-promoting monomers. *Polymer* **2009**, *50*, 4906−4916.

(6) Gienger, E. B.; Nguyen, P. A. T.; Chin, W.; Behler, K. D.; Snyder, J. F.; Wetzel, E. D. Microstructure and multifunctional properties of liquid+ polymer bicomponent structural electrolytes: Epoxy gels and porous monoliths. *J. Appl. Polym. Sci.* **2015**, *132*, No. 42681.

(7) Greenhalgh, E.; Ankersen, J.; Asp, L.; Bismarck, A.; Fontana, Q.; Houlle, M.; Kalinka, G.; Kucernak, A.; Mistry, M.; Nguyen, S.; Qian, H.; Shaffer, M.; Shirshova, N.; Steinke, J.; Wienrich, M. Mechanical, electrical and microstructural characterisation of multifunctional structural power composites. *J. Compos. Mater.* **2015**, *49*, 1823−1834.

(8) Johannisson, W.; Ihrner, N.; Zenkert, D.; Johansson, M.; Carlstedt, D.; Asp, L. E.; Sieland, F. Multifunctional performance of a carbon fiber UD lamina electrode for structural batteries. *Compos. Sci. Technol.* **2018**, *168*, 81−87.

(9) Carlstedt, D.; Asp, L. E. Performance analysis framework for structural battery composites in electric vehicles. *Composites, Part B* **2020**, *186*, No. 107822.
(10) Fan, J.; Shi, Z.; Tian, M.; Yin, J. Graphene−aramid nanofiber nanocomposite paper with high mechanical and electrical performance. *RSC Adv.* **2013**, *3*, 17664−17667.
(11) Shirshova, N.; Qian, H.; Shaffer, M. S. P.; Steinke, J. H. G.; Greenhalgh, E. S.; Curtis, P. T.; Kucernak, A.; Bismarck, A. Structural composite supercapacitors. *Composites, Part A* **2013**, *46*, 96−107.
(12) Ling, Z.; Ren, C. E.; Zhao, M.-Q.; Yang, J.; Giammarco, J. M.; Qiu, J.; Barsoum, M. W.; Gogotsi, Y. Flexible and conductive MXene films and nanocomposites with high capacitance. *Proc. Natl. Acad. Sci.* **2014**, *111*, 16676−16681.
(13) Peng, X.; Peng, L.; Wu, C.; Xie, Y. Two dimensional nanomaterials for flexible supercapacitors. *Chem. Soc. Rev.* **2014**, *43*, 3303−3323.
(14) Shirshova, N.; Qian, H.; Houllé, M.; Steinke, J. H.; Kucernak, A. R.; Fontana, Q. P.; Greenhalgh, E. S.; Bismarck, A.; Shaffer, M. S. Multifunctional structural energy storage composite supercapacitors. *Faraday Discuss.* **2014**, *172*, 81−103.
(15) An, H.; Mike, J.; Smith, K. A.; Swank, L.; Lin, Y.-H.; L. Pesek, S.; Verduzco, R.; Lutkenhaus, J. L. Highly Flexible Self-Assembled V2O5 Cathodes Enabled by Conducting Diblock Copolymers. *Sci. Rep.* **2015**, *5*, No. 14166.
(16) Guo, X.; Zheng, S.; Zhang, G.; Xiao, X.; Li, X.; Xu, Y.; Xue, H.; Pang, H. Nanostructured graphene-based materials for flexible energy storage. *Energy Storage Mater.* **2017**, *9*, 150−169.
(17) Liu, W.; Song, M.-S.; Kong, B.; Cui, Y. Flexible and Stretchable Energy Storage: Recent Advances and Future. *Perspectives* **2017**, *29*, No. 1603436.
(18) Yao, B.; Zhang, J.; Kou, T.; Song, Y.; Liu, T.; Li, Y. Paper-Based Electrodes for Flexible Energy Storage Devices. *Adv. Sci.* **2017**, *4*, No. 1700107.
(19) Meng, C.; Muralidharan, N.; Teblum, E.; Moyer, K. E.; Nessim, G. D.; Pint, C. L. Multifunctional Structural Ultrabattery Composite. *Nano Lett.* **2018**, *18*, 7761−7768.
(20) Shi, C.; Wang, T.; Liao, X.; Qie, B.; Yang, P.; Chen, M.; Wang, X.; Srinivasan, A.; Cheng, Q.; Ye, Q.; Li, A. C.; Chen, X.; Yang, Y. Accordion-like stretchable Li-ion batteries with high energy density. *Energy Storage Mater.* **2019**, *17*, 136−142.
(21) Kwon, S. R.; Harris, J.; Zhou, T.; Loufakis, D.; Boyd, J. G.; Lutkenhaus, J. L. Mechanically Strong Graphene/Aramid Nanofiber Composite Electrodes for Structural Energy and Power. *ACS Nano* **2017**, *11*, 6682−6690.
(22) Zhu, Y.; Murali, S.; Cai, W.; Li, X.; Suk, J. W.; Potts, J. R.; Ruoff, R. S. Graphene and Graphene Oxide: Synthesis, Properties, and Applications. *Adv. Mater.* **2010**, *22*, 3906−3924.
(23) Dikin, D. A.; Stankovich, S.; Zimney, E. J.; Piner, R. D.; Dommett, G. H. B.; Evmenenko, G.; Nguyen, S. T.; Ruoff, R. S. Preparation and characterization of graphene oxide paper. *Nature* **2007**, *448*, 457−460.
(24) Huang, S.-Y.; Le, P.-A.; Yen, P.-J.; Lu, Y.-C.; Sahoo, S. K.; Cheng, H.-W.; Chiu, P.-W.; Tseng, T.-Y.; Wei, K.-H. Cathodic plasma−induced syntheses of graphene nanosheet/MnO2/WO3 architectures and their use in supercapacitors. *Electrochim. Acta* **2020**, *342*, No. 136043.
(25) Le, P.-A.; Nguyen, V.-T.; Yen, P.-J.; Tseng, T.-Y.; Wei, K.-H. A new redox phloroglucinol additive incorporated gel polymer electrolyte for flexible symmetrical solid-state supercapacitors. *Sustainable Energy Fuels* **2019**, *3*, 1536−1544.
(26) Yang, M.; Cao, K.; Sui, L.; Qi, Y.; Zhu, J.; Waas, A.; Arruda, E. M.; Kieffer, J.; Thouless, M. D.; Kotov, N. A. Dispersions of Aramid Nanofibers: A New Nanoscale Building Block. *ACS Nano* **2011**, *5*, 6945−6954.
(27) Yang, M.; Cao, K.; Yeom, B.; Thouless, M.; Waas, A.; Arruda, E. M.; Kotov, N. A. Aramid nanofiber-reinforced transparent nanocomposites. *J. Compos. Mater.* **2015**, *49*, 1873−1879.
(28) Lyu, J.; Wang, X.; Liu, L.; Kim, Y.; Tanyi, E. K.; Chi, H.; Feng, W.; Xu, L.; Li, T.; Noginov, M. A.; Uher, C.; Hammig, M. D.; Kotov, N. A. High Strength Conductive Composites with Plasmonic Nanoparticles Aligned on Aramid Nanofibers. *Adv. Funct. Mater.* **2016**, *26*, 8435−8445.
(29) Lyu, J.; Hammig, M. D.; Liu, L.; Xu, L.; Chi, H.; Uher, C.; Li, T.; Kotov, N. A. Stretchable conductors by kirigami patterning of aramid-silver nanocomposites with zero conductance gradient. *Appl. Phys. Lett.* **2017**, *111*, No. 161901.
(30) Zhu, J.; Yang, M.; Emre, A.; Bahng, J. H.; Xu, L.; Yeom, J.; Yeom, B.; Kim, Y.; Johnson, K.; Green, P.; Kotov, N. A. Branched Aramid Nanofibers. *Angew. Chem., Int. Ed.* **2017**, *56*, 11744−11748.
(31) Flouda, P.; Feng, X.; Boyd, J. G.; Thomas, E. L.; Lagoudas, D. C.; Lutkenhaus, J. L. Interfacial Engineering of Reduced Graphene Oxide for Aramid Nanofiber-Enabled Structural Supercapacitors. *Batteries Supercaps* **2019**, *2*, 464−472.
(32) Flouda, P.; Shah, S. A.; Lagoudas, D. C.; Green, M. J.; Lutkenhaus, J. L. Highly Multifunctional Dopamine-Functionalized Reduced Graphene Oxide Supercapacitors. *Matter* **2019**, *1*, 1532−1546.
(33) Flouda, P.; Yun, J.; Loufakis, D.; Shah, S. A.; Green, M. J.; Lagoudas, D. C.; Lutkenhaus, J. L. Structural reduced graphene oxide supercapacitors mechanically enhanced with tannic acid. *Sustainable Energy Fuels* **2020**, 2301−2308.
(34) El-Kady, M. F.; Strong, V.; Dubin, S.; Kaner, R. B. Laser Scribing of High-Performance and Flexible Graphene-Based Electrochemical Capacitors. *Science* **2012**, *335*, 1326−1330.
(35) Persson, K.; Sethuraman, V. A.; Hardwick, L. J.; Hinuma, Y.; Meng, Y. S.; van der Ven, A.; Srinivasan, V.; Kostecki, R.; Ceder, G. Lithium Diffusion in Graphitic Carbon. *J. Phys. Chem. Lett.* **2010**, *1*, 1176−1180.
(36) Fan, Z.; Yan, J.; Zhi, L.; Zhang, Q.; Wei, T.; Feng, J.; Zhang, M.; Qian, W.; Wei, F. A three-dimensional carbon nanotube/graphene sandwich and its application as electrode in supercapacitors. *Adv. Mater.* **2010**, *22*, 3723−3728.
(37) Yu, D.; Dai, L. Self-assembled graphene/carbon nanotube hybrid films for supercapacitors. *J. Phys. Chem. Lett.* **2010**, *1*, 467−470.
(38) Wei, W.; Chen, W.; Ding, L.; Cui, S.; Mi, L. Construction of hierarchical three-dimensional interspersed flower-like nickel hydroxide for asymmetric supercapacitors. *Nano Research* **2017**, *10*, 3726−3742.
(39) Wei, W.; Ye, W.; Wang, J.; Huang, C.; Xiong, J.-B.; Qiao, H.; Cui, S.; Chen, W.; Mi, L.; Yan, P. Hydrangea-like α-Ni1/3Co2/3(OH)2 Reinforced by Ethyl Carbamate "Rivet" for All-Solid-State Supercapacitors with Outstanding Comprehensive Performance. *ACS Appl. Mater. Interfaces* **2019**, *11*, 32269−32281.
(40) Patel, A. G.; Johnson, L.; Arroyave, R.; Lutkenhaus, J. L. Design of multifunctional supercapacitor electrodes using an informatics approach. *Mol. Syst. Des. Eng.* **2019**, *4*, 654−663.
(41) Cheng, Q.; Tang, J.; Ma, J.; Zhang, H.; Shinya, N.; Qin, L.-C. Graphene and carbon nanotube composite electrodes for supercapacitors with ultra-high energy density. *Phys. Chem. Chem. Phys.* **2011**, *13*, 17615−17624.
(42) Pham, D. T.; Lee, T. H.; Luong, D. H.; Yao, F.; Ghosh, A.; Le, V. T.; Kim, T. H.; Li, B.; Chang, J.; Lee, Y. H. Carbon Nanotube-Bridged Graphene 3D Building Blocks for Ultrafast Compact Supercapacitors. *ACS Nano* **2015**, *9*, 2018−2027.
(43) Gupta, V.; Miura, N. Polyaniline/single-wall carbon nanotube (PANI/SWCNT) composites for high performance supercapacitors. *Electrochim. Acta* **2006**, *52*, 1721−1726.
(44) Yu, D.; Dai, L. Self-Assembled Graphene/Carbon Nanotube Hybrid Films for Supercapacitors. *J. Phys. Chem. Lett.* **2010**, *1*, 467−470.
(45) Fan, Z.; Yan, J.; Zhi, L.; Zhang, Q.; Wei, T.; Feng, J.; Zhang, M.; Qian, W.; Wei, F. A Three-Dimensional Carbon Nanotube/Graphene Sandwich and Its Application as Electrode in Supercapacitors. *Adv. Mater.* **2010**, *22*, 3723−3728.
(46) Hu, S.; Rajamani, R.; Yu, X. Flexible solid-state paper based carbon nanotube supercapacitor. *Appl. Phys. Lett.* **2012**, *100*, No. 104103.

https://dx.doi.org/10.1021/acsaem.0c01926
ACS Appl. Energy Mater. 2020, 3, 11763−11771

(47) Ebbesen, T. W.; Lezec, H. J.; Hiura, H.; Bennett, J. W.; Ghaemi, H. F.; Thio, T. Electrical conductivity of individual carbon nanotubes. *Nature* **1996**, *382*, 54−56.
(48) Kwon, S. R.; Elinski, M. B.; Batteas, J. D.; Lutkenhaus, J. L. Robust and Flexible Aramid Nanofiber/Graphene Layer-by-Layer Electrodes. *ACS Appl. Mater. Interfaces* **2017**, *9*, 17125−17135.
(49) Tubes, C. https://www.cheaptubes.com/product-category/functionalized-carbon-nanotubes/cooh-functionalized-carbon-nanotubes/.
(50) Björk, J.; Hanke, F.; Palma, C.-A.; Samori, P.; Cecchini, M.; Persson, M. Adsorption of Aromatic and Anti-Aromatic Systems on Graphene through $\pi-\pi$ Stacking. *J. Phys. Chem. Lett.* **2010**, *1*, 3407−3412.
(51) Medhekar, N. V.; Ramasubramaniam, A.; Ruoff, R. S.; Shenoy, V. B. Hydrogen Bond Networks in Graphene Oxide Composite Paper: Structure and Mechanical Properties. *ACS Nano* **2010**, *4*, 2300−2306.
(52) Wu, T.-M.; Lin, Y.-W.; Liao, C.-S. Preparation and characterization of polyaniline/multi-walled carbon nanotube composites. *Carbon* **2005**, *43*, 734−740.
(53) Che, J.; Chen, P.; Chan-Park, M. B. High-strength carbon nanotube buckypaper composites as applied to free-standing electrodes for supercapacitors. *J. Mater. Chem. A* **2013**, *1*, 4057−4066.
(54) Cheng, Y.; Lu, S.; Zhang, H.; Varanasi, C. V.; Liu, J. Synergistic Effects from Graphene and Carbon Nanotubes Enable Flexible and Robust Electrodes for High-Performance Supercapacitors. *Nano Lett.* **2012**, *12*, 4206−4211.
(55) Lee, W. S. V.; Peng, E.; Choy, D. C.; Xue, J. M. Mechanically robust glucose strutted graphene aerogel paper as a flexible electrode. *J. Mater. Chem. A* **2015**, *3*, 19144−19147.
(56) Li, S.; Zhao, C.; Shu, K.; Wang, C.; Guo, Z.; Wallace, G. G.; Liu, H. Mechanically strong high performance layered polypyrrole nano fibre/graphene film for flexible solid state supercapacitor. *Carbon* **2014**, *79*, 554−562.
(57) Li, Y.; Ren, G.; Zhang, Z.; Teng, C.; Wu, Y.; Lu, X.; Zhu, Y.; Jiang, L. A strong and highly flexible aramid nanofibers/PEDOT:PSS film for all-solid-state supercapacitors with superior cycling stability. *J. Mater. Chem. A* **2016**, *4*, 17324−17332.
(58) Ma, Y.; Li, P.; Sedloff, J. W.; Zhang, X.; Zhang, H.; Liu, J. Conductive Graphene Fibers for Wire-Shaped Supercapacitors Strengthened by Unfunctionalized Few-Walled Carbon Nanotubes. *ACS Nano* **2015**, *9*, 1352−1359.
(59) Muralidharan, N.; Teblum, E.; Westover, A. S.; Schauben, D.; Itzhak, A.; Muallem, M.; Nessim, G. D.; Pint, C. L. Carbon Nanotube Reinforced Structural Composite Supercapacitor. *Sci. Rep.* **2018**, *8*, No. 17662.
(60) Reece, R.; Lekakou, C.; Smith, P. A. A structural supercapacitor based on activated carbon fabric and a solid electrolyte. *Mater. Sci. Technol.* **2019**, *35*, 368−375.
(61) Rigueur, J. L.; Hasan, S. A.; Mahajan, S. V.; Dickerson, J. H. Buckypaper fabrication by liberation of electrophoretically deposited carbon nanotubes. *Carbon* **2010**, *48*, 4090−4099.
(62) Sumboja, A.; Foo, C. Y.; Wang, X.; Lee, P. S. Large Areal Mass, Flexible and Free-Standing Reduced Graphene Oxide/Manganese Dioxide Paper for Asymmetric Supercapacitor Device. *Adv. Mater.* **2013**, *25*, 2809−2815.
(63) Wang, D.-W.; Li, F.; Zhao, J.; Ren, W.; Chen, Z.-G.; Tan, J.; Wu, Z.-S.; Gentle, I.; Lu, G. Q.; Cheng, H.-M. Fabrication of Graphene/Polyaniline Composite Paper via In Situ Anodic Electropolymerization for High-Performance Flexible Electrode. *ACS Nano* **2009**, *3*, 1745−1752.
(64) Weng, Z.; Su, Y.; Wang, D.-W.; Li, F.; Du, J.; Cheng, H.-M. Graphene−Cellulose Paper Flexible Supercapacitors. *Adv. Energy Mater.* **2011**, *1*, 917−922.
(65) Whitten, P. G.; Spinks, G. M.; Wallace, G. G. Mechanical properties of carbon nanotube paper in ionic liquid and aqueous electrolytes. *Carbon* **2005**, *43*, 1891−1896.
(66) Zhang, X.; Sui, Z.; Xu, B.; Yue, S.; Luo, Y.; Zhan, W.; Liu, B. Mechanically strong and highly conductive graphene aerogel and its use as electrodes for electrochemical power sources. *J. Mater. Chem.* **2011**, *21*, 6494−6497.
(67) Sun, W.; Shah, S. A.; Lowery, J. L.; Oh, J. H.; Lutkenhaus, J. L.; Green, M. J. Lightweight Kevlar-Reinforced Graphene Oxide Architectures with High Strength for Energy Storage. *Adv. Mater. Interfaces* **2019**, *6*, No. 1900786.
(68) Kim, S. Y.; Hong, J.; Kavian, R.; Lee, S. W.; Hyder, M. N.; Shao-Horn, Y.; Hammond, P. T. Rapid fabrication of thick spray-layer-by-layer carbon nanotube electrodes for high power and energy devices. *Energy Environ. Sci.* **2013**, *6*, 888−897.
(69) Barisci, J. N.; Wallace, G. G.; Baughman, R. H. Electrochemical studies of single-wall carbon nanotubes in aqueous solutions. *J. Electroanal. Chem.* **2000**, *488*, 92−98.
(70) Shah, S. A.; Kulhanek, D.; Sun, W.; Zhao, X.; Yu, S.; Parviz, D.; Lutkenhaus, J. L.; Green, M. J. Aramid nanofiber-reinforced three-dimensional graphene hydrogels for supercapacitor electrodes. *J. Colloid Interface Sci.* **2020**, *560*, 581−588.

https://dx.doi.org/10.1021/acsaem.0c01926
ACS Appl. Energy Mater. 2020, 3, 11763−11771